Generated carrier dynamics in V-pit enhanced InGaN/GaN light emitting diode

Journal:	*ACS Photonics*
Manuscript ID	ph-2017-00944j.R2
Manuscript Type:	Article
Date Submitted by the Author:	18-Dec-2017

Complete List of Authors:	Ajia, Idris ; King Abdullah University of Science and Technology, Physical Sciences and Engineering Division Edwards, Paul; University of Strathclyde, Department of Physics Pak, Yusin; King Abdullah University of Science and Technology, Physical Sciences and Engineering Division Belekov, Ermek.; King Abdullah University of Science and Technology Roldan, Manuel; King Abdullah University of Science and Technology, Imaging and Characterization Laboratory Wei, Nini; King Abdullah University of Science and Technology, Imaging and Characterization Laboratory Liu, Zhiqiang; Semiconductor Lighting Technology Research and Development Center, Institute of Semiconductors, Chinese Academy of Sciences Martin, Robert; Strathclyde University, Department of Physics Roqan, Iman; King Abdullah University of Science and Technology,

Generated carrier dynamics in V-pit enhanced InGaN/GaN light emitting diode

Idris A. Ajia[†]; Paul R. Edwards[‖], Yusin Pak[†], Ermek Belekov[†]; Manuel A. Roldan[‡]; Nini Wei[‡]; Zhiqiang Liu[§], Robert W. Martin[‖] and Iman S. Roqan[†,*]

[†]King Abdullah University of Science and Technology (KAUST), Physical Science and Engineering Division, Thuwal, Saudi Arabia.

[‡]King Abdullah University of Science and Technology (KAUST), Imaging and Characterization Core Laboratory, Thuwal, Saudi Arabia.

[‖]Department of Physics, SUPA, University of Strathclyde, Glasgow, G4 0NG, United Kingdom.

[§]Development Center, Institute of Semiconductors, Chinese Academy of Sciences, Beijing, China.

*E-mail: Iman.roqan@kaust.edu.sa

Abstract

We investigate the effects of V-pits on the optical properties of a state-of-the art highly efficient, blue InGaN/GaN multi-quantum-well (MQW) light emitting diode (LED) with high internal quantum efficiency (IQE) of > 80%. The LED is structurally enhanced by incorporating pre-MQW InGaN strain-relief layer with low InN content and patterned sapphire substrate. For comparison, a conventional (unenhanced) InGaN/GaN MQW LED (with IQE of 46%) grown under similar conditions was subjected to the same measurements. Scanning transmission electron microscopy (STEM) reveals the absence of V-pits in the unenhanced LED, whereas in the enhanced LED, V-pits with $\{10\bar{1}1\}$ facets, emerging from threading dislocations (TDs) were prominent. Cathodoluminescence mapping reveals the luminescence properties near the V-pits, showing that the formation of V-pit defects can

encourage the growth of defect-neutralizing barriers around TD defect states. The diminished contribution of TDs in the MQWs allows indium-rich localization sites to act as efficient recombination centers. Photoluminescence and time-resolved spectroscopy measurements suggest that the V-pits play a significant role in the generated carrier rate and droop mechanism, showing that the quantum confined Stark effect is suppressed at low generated carrier density, after which the carrier dynamics and droop are governed by the carrier overflow effect.

Keywords InGaN, efficiency droop, light emitting diode, carrier dynamics, time-resolved spectroscopy

Blue light emitting diodes (LEDs) based on III-nitrides materials are distinguished by their structural and mechanical robustness and their inherently efficient radiative recombination rates.[1-2] At high carrier injection rates, however, InGaN LEDs suffer from an efficiency droop,[2-10] which limits their performance. According to the prevalent consensus, Auger recombination is the cause of the droop.[6-8] However, some researchers have also attributed this droop to the presence of polarization fields in the active layers, which facilitate electron leakage into the p-GaN layer.[9, 11-12] In fact, it has been suggested that these effects might not be mutually exclusive.[10] To mitigate the deleterious effects of the droop, researchers have experimented on several structural improvements. One of the most prominent efforts focused on a patterned sapphire substrate (PSS) that results in stress relaxation of the GaN epilayers and the reduction of TD density, leading to efficiency improvement.[13-16] Other approaches, based on inclusion of p-AlGaN [17-18] or p-InGaN/AlGaN [19] electron blocking layers (EBL) above the multi-quantum-well (MQW) LED structure, were found to enhance efficiency. Additionally, incorporation of InGaN/GaN strain-relief layers, such as strained-layer superlattices (SLSs) or low InN content layers, have been explored as a means to increase InGaN LED efficiency by suppressing built-in polarization fields in the MQW region.[20-22] SLS layers have previously been used to regulate the growth of thin quantum wells in V-pits with characteristic $\{10\bar{1}1\}$ facets.[23-25] However, the effects of V-pits on the carrier dynamics and droop mechanism in III-nitride LEDs are presently not fully understood.

In this work, we show the optical properties of the LED structure near such V-pits and the effect of generated carriers on the optical efficiency and droop phenomenon. For comparison, we also examine a conventional MQW LED grown on a flat substrate without the strain relief layer. Thus, the present study advances the current understanding of the carrier dynamics and droop effects in LEDs.

EXPERIMENTAL DETAILS

Two blue-emitting $In_xGa_{1-x}N$/GaN LED structures (nominal x ≈ 0.15) were prepared by metalorganic chemical vapor deposition (MOCVD). The structurally enhanced LED sample (denoted as LED1) was grown on PSS (lens-shaped patterns of ~2 µm diameter) with a low InN content strain-relief layer and an EBL, whereas LED2 sample was grown as a conventional LED structure on a planar sapphire substrate without a strain-relief layer or EBL. We used trimethyl-indium (TMIn), trimethyl-gallium (TMGa), trimethyl-aluminum (TMAl) and NH_3. Both LED structures consisted of a low-temperature GaN buffer layer overgrown on the substrates, followed by an undoped GaN layer of 3 µm thickness. In the next step, a 3-µm thick n-GaN layer was grown, followed by an 8-period InGaN/GaN (3 nm/8 nm) MQW active layer capped by a p-GaN layer. In LED1, a strain-relief layer was inserted between the n-GaN layer and the InGaN/GaN MQW active region. A p-AlGaN EBL was sandwiched between the p-GaN layer and the MQWs of LED1. For I-V and electroluminescence (EL) characterization, the LEDs were fabricated by inductively coupled plasma (ICP) etching to expose the n-GaN layer. Prior to ICP etching, a 500 nm SiO_2 protective layer was grown on part of the p-GaN layer. This SiO_2 layer was then after, etched away using buffered oxide etchant (BOE) to expose the p-GaN layer. Ni/Au (5/5 nm) current spreading layer was deposited on the p-GaN layers, following which Au (150 nm) and Ti/Al/Ni/Au (10/100/30/100 nm) electrodes were subsequently deposited on the exposed p-GaN and n-GaN layers, respectively. A Keithley DC power supply was used as the voltage source for IV measurements, and ReRa solutions Tracer IV-curve software was used for data acquisition (Figure S5, supporting information).

The LED samples were prepared for scanning transmission electron microscopy (STEM) and high angle annular dark field-scanning TEM images (HAADF-STEM) using an FEI Quanta 3D focused Ion Beam (FIB)-Scanning Electron Microscope (SEM). The HAADF-STEM images were acquired using a Cs-Probe Corrected FEI Titan, operated at an acceleration voltage of 300 kV. We estimated the V-pit density after etching the p-layer and EBL by FIB-SEM. Cathodoluminescence (CL) mapping was acquired at room temperature (RT) using an FEI Sirion 200 FEGSEM attached to monochromator with 400 l/mm grating.[26] The electron beam energy was fixed at 10 keV for CL mapping. For power-

dependent RT-photoluminescence (PL) measurements, the second harmonic line (400 nm) of an ultrafast (150 fs) Ti:Sapphire laser (76 MHz) was used. For temporally resolved RT-PL (TRPL) measurements, an APE GmbH pulse picker was used to reduce the pulse frequency to 1 MHz. The diameter of the incident beam was ~ 60 μm. A charge-coupled device camera attached to a Hamamatsu single-sweep streak camera was used to acquire both the temporal and time integrated responses. The samples were mounted in a closed-cycle helium cryostat for low temperature (5 K) measurements.

RESULTS AND DISCUSSION

Figure 1(a) shows the cross-sectional STEM images of the LED1. We observe a TD defect (circled area) emerge from the center of the V-pit defect into the p-GaN layer of the sample. SEM images reveal that the average V-pit density is ≈ 1.5 × 10^8 cm^{-2} as shown in Figure S2 of the Supporting Information.[27] The facets of the V-pit walls are separated by a ≈ 63° angle, which coincides with the angle separating the $\{10\bar{1}1\}$ group of planes of hexagonal InGaN structures.[28-29] The STEM image shows that the V-pit walls are characterized by quantum well and barrier thinning, in line with previous observations.[23-24] It is well known that different planer facets of III-nitride based crystal lattices have different surface energies,[30-31] which can lead to strong dependence of adatom kinetics on the crystal plane orientation.[32] Indeed, it was shown by Hangleiter, *et al*.[25] demonstrated that the In growth rate along the semi-polar plane is slow, which would explain the MQW thinning. V-pits are not observed in LED2, as shown in Figure 1(b), where TDs can be seen cleaving through its MQWs.

We investigate the detailed emission spectrum of LED1 to study the effect of the V-pits. We plot the mean CL energy spectrum of LED1 emission (Figure 2(a)), showing that the main energy peak is centered at ~2.71 eV. The CL intensity maps corresponding to the color shaded energy regions are shown alongside the spectrum. The low energy InGaN shoulder, located in the 2.35–2.70 eV range, corresponds to the brighter areas on the CL map in Figure 2(b), while the dark spots are

signatures of the V-pits. The shoulder can be due to InN-rich fluctuations inside the MQWs. The bright regions shown in Figure 2(c) correspond to the MQW emission in the 2.75–2.90 eV range. In the same figure, the V-pit spots become smaller due to reduced InN content in the areas in the immediate vicinity of V-pits. The high energy shoulder located between 3.05 and 3.25 eV represents the emission from the V-pits (bright spots in the CL map of Figure 2(d)). It should be noted that the low InN layer is also located within this range, however its intensity is low enough to provide contrast for the inner walls of the V-pits due to the GaN quantum barrier above this layer (Figure S3, supporting material).[27] Figure 2(e) shows the CL map related to emission near the GaN bandedge (located at 3.35–3.50 eV), indicating that the V-pits become sparse, suggesting that p-GaN, the V-pit walls and the preceding GaN layers may have contributed to this peak.

In Figure 3(a) and (b), we compare the hyperspectral CL intensity maps of LED1 and LED2, respectively, integrated over the 2.4–2.9 eV energy range Unlike in LED1, we find no evidence of V-pits in LED2 and large sections of low CL intensity are shown (Figure 3(b)) overshadowing patches of high intensity regions. Figure 3(c) and (d) show the corresponding CL spectra of the regions annotated as A and B, in the CL maps (Figure 3(a) and 3(b), respectively). A high energy shoulder peak at ≈3.03 eV that is related to well-barrier intermixing (Figure 2(d)) in LED1 is absent from the LED2 emission spectrum and no significant spectral distinctions exist between the dark and bright regions due to the absence of such V-pits. Figure 3(e) and (f) show the correlations between the LED centroid energy and the CL intensity (integrated over the 2.4–3.2 eV range). Figure 3(e) indicates a clear inverse correlation between the peak energy and CL intensity in LED1. This correlation leads us to deduce that the V-pits, corresponding to the high energy shoulder (Figure 2(d) and Figure 3(c)), act as dislocation terminals. The walls of V-pits are known to act as TD passivating barriers, due to thinner MQW walls on the facets of the pits.[21, 25, 33] Well-barrier intermixing inside of the v-pits may also play a role in the TD passivation according to Pereira, *et al.* [30], however we were not able to determine the extent of this from EDX results, as shown in figure S7 and S8 of supporting information. Additionally, the regions with lower peak energy also show

higher intensity (represented in Figure 2(c)) relative to the high energy shoulder, suggesting a higher efficiency of radiative recombination processes within InN-rich potentials in the MQWs. In contrast, Figure 3(f) shows a positive correlation between mean peak energy and CL intensity in LED2, implying that CL quenching occurs around InN-rich sites. This finding indicates that, in the absence of TD passivating V-pits, InN tends to accumulate near TD sites.[34-35]

We investigate the radiative recombination efficiency of the carriers and the nature of the droop in the enhanced LED (LED1) compared to the conventional one (LED2), by conducting power-dependent PL measurements at RT and interpreting the results using the Shockley-Read-Hall (SRH) model.[36-37] The rate equation of generated carriers, $G\ (cm^{-3}s^{-1})$, in steady state is given by:

$$G = An + Bn^2 + Cn^3 \quad (1)$$

where A, B and C are the coefficients of (non-radiative) Shockley-Read-Hall (SRH), radiative and Auger recombination, respectively. $G(cm^{-3}s^{-1})$ can then be estimated from the average excitation power value (P_{av}) as follows:

$$G(P) = \frac{P_{av} \times \tau_D \times \alpha \times (1-R)}{\tau_W \times A \times h\upsilon \times q} \quad (2)$$

where α is the absorption coefficient of InGaN, linearly extrapolated from the values for InN and GaN (SRH Method, supporting information),[27] R is the reflectivity of the GaN surface at 3.1 eV (10%),[38] τ_D is the pulse duration, τ_W is the pulse width, A denotes the area of the incident excitation beam, $h\upsilon$ is the laser photon energy, and q represents the elementary charge. It follows from Eq. (1) that the observed integrated luminescence intensity at RT, $I(P)$, of the samples is represented by the following equation:

$$I(P) = kBn^2 \quad (3)$$

where k is a constant related to the product of the spectrograph's collection efficiency and light extraction efficiency of the LEDs. Combining Eq. (1), (2) and (3), the LED internal quantum efficiencies (IQE), $\eta_{IQE}(P)$, can be determined by the ratio:

$$\eta_{IQE}(P) = \frac{Bn^2}{G(P)} = \frac{I(P)}{k\,G(P)} \quad (4)$$

The value of *k* is estimated using the following steps. First, the number of parameters is reduced by restricting the analysis to low carrier generation rates ($G < 10^{31}$ $cm^{-3}s^{-1}$) where Auger recombination is negligible and thus allowing the third term in Eq. (1) to be eliminated.[39] Substituting for n from Eq. (3) gives the new equation, $G = \left({}^{A}/_{\sqrt{kB}}\right) I(P)^{\frac{1}{2}} + \left({}^{1}/_{k}\right) I(P)$, which was then fitted into a plot of *G(P)* versus the integrated luminescence intensity, *I(P)*, where *A*, *B* and *k* were treated as constant fitting parameters (Figure 3S, Supporting Information).[27] Finally, we estimated the value of $\eta_{IQE}(P)$ by substituting *k* into Eq. (4).

Figure 4(a) shows the carrier generation rate, G, dependence (in log scale) of IQE for both LEDs, excited by 400 nm (below the GaN bandgap). To interpret the IQE behavior of both LEDs, we define three prominent regions of interest (annotated as RI, RII and RIII Figure 4). Region RI follows the linear dependence of the SRH recombination (non-radiative) rate (*An*) with G. In the range of this measurement, the RI region is observed in LED2 for $4.5\times10^{27} < G < 8.6\times10^{28}$ $cm^{-3}s^{-1}$, whereas this region is not observed in the structurally enhanced LED1. Since $\eta_{IQE}(P)$ is a function of radiative recombination (Eq. (4)), a slight increase in $\eta_{IQE}(P)$ of LED2 occurs because the main LED2 peak significantly overlaps with the defect band, which increases linearly with *G*, at low carrier density (Figure 4(d)). Such overlap is not observed at either low or high carrier densities in LED1 (Figure 4(c)). In the region denoted as RII ($4.5\times10^{27} < G < 6.7\times10^{29}$ $cm^{-3}s^{-1}$ for LED1 and $1.0\times10^{29} < G < 6.1\times10^{30}$ $cm^{-3}s^{-1}$ for LED2), $\eta_{IQE}(P)$ of both LEDs increases rapidly until it reaches a maximum value. This region seems more consistent with the radiative term (Bn^2) in Eq. (1). The maximum IQE for LED1 is > 80%, compared to 46% obtained for LED2. In the region denoted as RIII, there is a saturation in radiative efficiency and the droop effect occurs, where the IQE of both LEDs starts to decline, albeit at different G values. The droop effect commences at around $G \approx 2.3\times10^{30}$ $cm^{-3}s^{-1}$ for LED1, and at $G \approx 9.0\times10^{30}$ $cm^{-3}s^{-1}$ for LED2, consistent with the previously reported value of ~3.7×10^{31} $cm^{-3}s^{-1}$.[39] The commencement of the droop effect at lower generated carrier density in LED1 is most likely due to

the reduction in the effective MQW volume, as a result of high v-pit defect density. A similar observation was made by estimating the IQE of both LEDs by EL (Figure S6). In this case, the maximum IQE values for both LEDs were consistent with the PL results (a more detailed discussion of this measurement is provided in the supporting information. The internal quantum efficiency, $\eta_{IQE}(P)$, eventually declined to 48% and 30% at $G \approx 5.3\times10^{31}$ $cm^{-3}s^{-1}$ for LED1 and LED2, respectively. Furthermore, the inset of Figure 4(a) shows that the efficiency droop characteristics of the two LEDs behave differently as the excitation power intensity increases. The droop regime of LED2 follows a convex curve, likely attributed to the dominant effect of defect-related non-radiative recombination through the SRH process,[40] whereas that of LED1 follows a concave IQE curve, indicating that the droop could be due to the carrier overflow mechanism. When the effect of SRH recombination is significantly diminished, carrier overflow becomes the dominant source of efficiency droop.[40]

To further explain the droop behavior, we investigate the dependence of the peak energy of both LEDs on G (Figure 4(b)). We observe a clear blue-shift of ~80 meV in LED1 as the excitation power increases. However, the peak position of LED2 remains initially unchanged, before slightly blue-shifting by 10 meV at $G \approx 6.7\times10^{29}$ $cm^{-3}s^{-1}$. To understand these distinct behaviors, the full width at half maximum (FWHM) values of the emission peaks of both LEDs are plotted as a function of G (Figure 4(b), inset). For LED1, the peak FWHM decreases slightly (by 5 meV) as G increases from 4.5×10^{27} to 3.7×10^{28} $cm^{-3}s^{-1}$, before broadening by 30 meV to 155 meV at higher G values, followed by an invariant response to generated carriers, starting from $G \approx 5.2\times10^{30}$ $cm^{-3}s^{-1}$. For LED2, the FWHM initially decreases significantly (by 55 meV, from 165 meV to 110 meV for $4.5\times10^{27} < G < 1.0\times10^{29}$ $cm^{-3}s^{-1}$), before broadening by 43 meV as G increases. The FWHM narrows as the carrier density increases due to the screening of strain-induced electric field (i.e., quantum confined Stark effect (QCSE)) by the increasing carrier population. However, FWHM broadening accompanied by blue-shifting of the peak energy as carrier density increases is caused by carrier overflow from deeply localized InN-rich states to shallower states and other higher energy states. By this point, the QCSE is fully suppressed by the high carrier density.[41] Thus, the QCSE effect is not significant in LED1

and is overcome at low *G* value (10^{28} $cm^{-3}s^{-1}$). Consequently, its Auger dynamics are governed by the overflow effect. We therefore propose that, beyond the QCSE screening limit, the observed peak blue-shift in LED1 can be attributed to the carrier saturation of strong localization centers (due to indium segregation) and subsequent occupation of weak states inside the well,[42] followed by carrier occupation of states inside the V-pits. Given that the Auger effect of LED1 is barely affected by piezoelectric polarization, carrier overflow around the V-pits is suggested as the mechanism behind the characteristic concave droop behavior observed in LED1.[10, 40] This mechanism is illustrated in Figure 4(e). This assertion is supported by the fact that the droop effect commences at the same *G* value (≈ 10^{30} $cm^{-3}s^{-1}$) that the FWHM became constant. It is also plausible to assume that excess carriers may overflow into the p-GaN region as well.[40] However this effect should not be significant, since the excitation photon energy (3.1 eV) is markedly below the AlGaN EBL bandgap. For LED2, the limited dependence of the peak energy on carrier generation rate and the initial narrowing of its FWHM (Figure 4(b)) indicate that the carriers are already weakly confined, leaving excess carriers to contend with a nontrivial contribution from QCSE and the defect states of LED2. The FWHM of LED2 initially plateaus before starting to increase at high *G* (> 10^{29} $cm^{-3}s^{-1}$) values, indicating that the full screening of the QCSE in LED2 occurs at an additional order of magnitude than LED1, causing a slight blue-shift at $G \approx 6.7 \times 10^{29}$ $cm^{-3}s^{-1}$. Thus, LED2's Auger effect may have been affected by the continuous evolution of the electron-hole overlap ratio due to the dependence of its polarization field on injected carrier density, which explains its convex droop characteristic.[10]

Power-dependent TRPL was carried out to confirm the contribution of radiative and non-radiative recombination in LED1 compared to LED2. Fig. 5(a) and 5(b) respectively show the power-dependent TRPL lifetimes of LED1 and LED2 taken at 5 K. LED1 exhibits a non-exponential carrier lifetime decay (a similar behavior is observed at 290 K), suggesting presence of multi-state recombination paths, which can be approximated by the bi-exponential equation:[43]

$$Int(t) = A_f e^{-t/\tau_f} + A_s e^{-t/\tau_s}, \quad (5)$$

where A_f and A_s are, respectively, the fast and slow peak intensities at time t = 0, while τ_f and τ_s denote the decay lifetimes of the fast and slow decay components. However, LED2 exhibits a single exponential decay, suggesting that the excess carrier recombination paths in the two LEDs are different.

Figure 6 shows the PL decay lifetimes as a function of G at both 5 K and 290 K for LED1 and LED2, respectively. At 5 K, the PL lifetime of the LED1 peak declines from 96 ns to 47 ns for $6\times10^{27} < G < 2.7\times10^{28}$ $cm^{-3}s^{-1}$, after which it remains constant (Figure 6(a)). This inverse proportionality of radiative carrier lifetime to excitation carrier density implies that defect-related non-radiative recombination plays a negligible role at 5 K [17, 44]. However, at 290 K, the PL lifetime increases with G until 4.2×10^{28} $cm^{-3}s^{-1}$, which is due to the increase in non-radiative lifetime of LED1, as shown by the radiative and non-radiative lifetime in the inset of Figure 6(a). This behavior is followed by a subsequent reduction in the PL lifetime when radiative recombination starts to dominate the recombination process due to the saturation of non-radiative defect sites.[45] This behavior confirms that the non-radiative recombination processes become influential at high temperatures only, when thermal activation contributes to the deconfinement of previously confined carriers. Nonetheless, this effect occurs at low G values only ($G < 10^{29}$ $cm^{-3}s^{-1}$, IQE << 50%). For LED2, Figure 6(b) shows that the PL lifetime increases initially at 5 K (from 12 ns to 14 ns in the $6.0\times10^{27} < G < 1.8\times10^{28}$ $cm^{-3}s^{-1}$ range) before decreasing as G increases, whereas at 290 K its PL lifetime increases monotonously with G. There is a striking similarity between LED2's behavior at 5 K and that of LED1 at 290 K. Therefore, we posit that, at low excitation intensities, defect-related non-radiative recombination plays a prominent role in the recombination processes of LED2 at 5K. At RT, non-radiative processes dominate recombination rates beyond $G = 10^{29}$ $cm^{-3}s^{-1}$ (inset of Figure 6(b)). This finding is also supported by I-V plots (Figure S5, supporting information),[27] which show that the effect of shunt resistance was less severe in LED1 than in LED2. Shunt resistance is indicative of damaged regions or surface imperfections[17] which may result from dislocation defects.[46] These results confirm that the role of defect-related recombination was far less significant in LED1 than in LED2.

CONCLUSION

We investigated the carrier dynamics of a V-pit enhanced MQW LED. At low carrier densities, the V-pits acted as TD passivating barriers, thereby permitting efficient radiative recombination in the wells. However, as carrier density increases, the reduced effective volume of the MQWs allows for an early onset of Auger phenomenon. We further show that the Auger droop effect is mainly driven by carrier overflow, rather than piezoelectric polarization or SRH defects in the V-pit enhanced LED. Lifetime measurements show that the improved efficiency of the carrier recombination processes in the structurally enhanced LED was significantly aided by the presence of V-pits, leading to dominant radiative recombination process at RT.

ASSOCIATED CONTENT

Supporting information

Estimation of p-GaN doping concentration by SIMS; details of V-pit density estimation by SEM; G(P) vs I(P) plots and fittings; I-V characteristics and peak overlap explanation between the strain relief layer and the V-pits, electroluminescence IQE, off-center cut characteristics of V-pits, and EDX compositional mapping around the V-pits . This material is available free of charge via the Internet at http://pubs.acs.org.

AUTHOR INFORMATION

All authors have given approval to the final version of the manuscript.

Corresponding Author

*E-mail:iman.roqan@kaust.edu.sa

Notes

The authors declare no competing financial interest.

ACKNOWLEDGEMENTs

The authors thank King Abdullah University of Science and Technology for the financial support.

REFERENCES

1. Lester, S. D.; Ponce, F. A.; Craford, M. G.; Steigerwald, D. A., High dislocation densities in high efficiency GaN-based light-emitting diodes. *Appl. Phys. Lett.* **1995,** *66*, 1249-1251.

2. Yang, T.-J.; Shivaraman, R.; Speck, J. S.; Wu, Y.-R., The influence of random indium alloy fluctuations in indium gallium nitride quantum wells on the device behavior. *J. Appl. Phys.* **2014,** *116*, 113104.

3. Kim, A. Y.; Götz, W.; Steigerwald, D. A.; Wierer, J. J.; Gardner, N. F.; Sun, J.; Stockman, S. A.; Martin, P. S.; Krames, M. R.; Kern, R. S.; Steranka, F. M., Performance of High-Power AlInGaN Light Emitting Diodes. *physica status solidi (a)* **2001,** *188*, 15-21.

4. Takashi, M.; Motokazu, Y.; Shuji, N., Characteristics of InGaN-Based UV/Blue/Green/Amber/Red Light-Emitting Diodes. *Jpn. J. Appl. Phys.* **1999,** *38*, 3976.

5. Dong-Pyo, H.; Jong-In, S.; Dong-Soo, S.; Kyu-Sang, K., Effects of unbalanced carrier injection on the performance characteristics of InGaN light-emitting diodes. *Applied Physics Express* **2016,** *9*, 081002.

6. Shen, Y. C.; Mueller, G. O.; Watanabe, S.; Gardner, N. F.; Munkholm, A.; Krames, M. R., Auger recombination in InGaN measured by photoluminescence. *Appl. Phys. Lett.* **2007,** *91*, 141101.

7. Delaney, K. T.; Rinke, P.; Van de Walle, C. G., Auger recombination rates in nitrides from first principles. *Appl. Phys. Lett.* **2009,** *94*, 191109.

8. Iveland, J.; Martinelli, L.; Peretti, J.; Speck, J. S.; Weisbuch, C., Direct Measurement of Auger Electrons Emitted from a Semiconductor Light-Emitting Diode under Electrical Injection: Identification of the Dominant Mechanism for Efficiency Droop. *Phys. Rev. Lett.* **2013,** *110*, 177406.

9. Kim, M.-H.; Schubert, M. F.; Dai, Q.; Kim, J. K.; Schubert, E. F.; Piprek, J.; Park, Y., Origin of efficiency droop in GaN-based light-emitting diodes. *Appl. Phys. Lett.* **2007,** *91*, 183507.

10. Piprek, J.; Römer, F.; Witzigmann, B., On the uncertainty of the Auger recombination coefficient extracted from InGaN/GaN light-emitting diode efficiency droop measurements. *Appl. Phys. Lett.* **2015,** *106*, 101101.

11. Fu, H.; Lu, Z.; Zhao, Y., Analysis of low efficiency droop of semipolar InGaN quantum well light-emitting diodes by modified rate equation with weak phase-space filling effect. *AIP Advances* **2016,** *6*, 065013.

12. Ryu, H.-Y.; Shin, D.-S.; Shim, J.-I., Analysis of efficiency droop in nitride light-emitting diodes by the reduced effective volume of InGaN active material. *Appl. Phys. Lett.* **2012,** *100*, 131109.

13. Gao, H.; Yan, F.; Zhang, Y.; Li, J.; Zeng, Y.; Wang, G., Improvement of the performance of GaN-based LEDs grown on sapphire substrates patterned by wet and ICP etching. *Solid·State Electron.* **2008,** *52*, 962-967.

14. Tadatomo, K.; Okagawa, H.; Ohuchi, Y.; Tsunekawa, T.; Jyouichi, T.; Imada, Y.; Kato, M.; Kudo, H.; Taguchi, T., High Output Power InGaN Ultraviolet Light-Emitting Diodes Fabricated on Patterned Substrates Using Metalorganic Vapor Phase Epitaxy. *physica status solidi (a)* **2001,** *188*, 121-125.

15. Lee, K.; Lee, H.; Lee, C.-R.; Kim, J. S.; Lee, J. H.; Ryu, M.-Y.; Leem, J.-Y., Spatial emission distribution of InGaN/GaN light-emitting diodes depending on the pattern structures. *Mater. Res. Bull.* **2014,** *58*, 121-125.

16. Lee, Y.-C.; Yeh, S.-C.; Chou, Y.-Y.; Tsai, P.-J.; Pan, J.-W.; Chou, H.-M.; Hou, C.-H.; Chang, Y.-Y.; Chu, M.-S.; Wu, C.-H.; Ho, C.-H., High-efficiency InGaN-based LEDs grown on patterned sapphire substrates using nanoimprinting technology. *Microelectronic Engineering* **2013,** *105*, 86-90.

17. Schubert, E. F., *Light-emitting diodes*. 2nd ed.; Cambridge University Press: Cambridge ; New York, 2006; p x, 422 p.

18. Yu, C.-T.; Lai, W.-C.; Yen, C.-H.; Chang, S.-J., Effects of InGaN layer thickness of AlGaN/InGaN superlattice electron blocking layer on the overall efficiency and efficiency droops of GaN-based light emitting diodes. *Optics Express* **2014,** *22*, A663-A670.

19. Liu, Z.; Ma, J.; Yi, X.; Guo, E.; Wang, L.; Wang, J.; Lu, N.; Li, J.; Ferguson, I.; Melton, A., p-InGaN/AlGaN electron blocking layer for InGaN/GaN blue light-emitting diodes. *Appl. Phys. Lett.* **2012,** *101*, 261106.

20. Ju, J.-W.; Kang, E.-S.; Kim, H.-S.; Jang, L.-W.; Ahn, H.-K.; Jeon, J.-W.; Leea, I.-H.; Baek, J. H., Metal-organic chemical vapor deposition growth of InGaN/GaN high power green light emitting diode: Effects of InGaN well protection and electron reservoir layer. *J. Appl. Phys.* **2007,** *102*, 053519.

21. Leem, S. J.; Shin, Y. C.; Kim, K. C.; Kim, E. H.; Sung, Y. M.; Moon, Y.; Hwang, S. M.; Kim, T. G., The effect of the low-mole InGaN structure and InGaN/GaN strained layer superlattices on optical performance of multiple quantum well active layers. *J. Cryst. Growth* **2008,** *311*, 103-106.

22. Davies, M. J.; Dawson, P.; Massabuau, F. C.-P.; Oliver, R. A.; Kappers, M. J.; Humphreys, C. J., The effects of Si-doped prelayers on the optical properties of InGaN/GaN single quantum well structures. *Appl. Phys. Lett.* **2014,** *105*, 092106.

23. Chang, C.-Y.; Li, H.; Shih, Y.-T.; Lu, T.-C., Manipulation of nanoscale V-pits to optimize internal quantum efficiency of InGaN multiple quantum wells. *Appl. Phys. Lett.* **2015,** *106*, 091104.

24. Tomiya, S.; Kanitani, Y.; Tanaka, S.; Ohkubo, T.; Hono, K., Atomic scale characterization of GaInN/GaN multiple quantum wells in V-shaped pits. *Appl. Phys. Lett.* **2011,** *98*, 181904.

25. Hangleiter, A.; Hitzel, F.; Netzel, C.; Fuhrmann, D.; Rossow, U.; Ade, G.; Hinze, P., Suppression of Nonradiative Recombination by V-Shaped Pits in GaInN/GaN Quantum Wells Produces a Large Increase in the Light Emission Efficiency. *Phys. Rev. Lett.* **2005,** *95*, 127402.

26. Paul, R. E.; Robert, W. M., Cathodoluminescence nano-characterization of semiconductors. *Semicond. Sci. Tech.* **2011,** *26*, 064005.

27. Supporting information: V-pit density estimation by SEM, G(P) vs I(P) plots and fittings, and estimation of doping p-GaN doping concentration by SIMS, I-V Characteristics.

28. Bessolov, V. N.; Konenkova, E. V.; Kukushkin, S. A.; Osipov, A. V.; Rodin, S. N., Semipolar Gallium Nitride on Silicon: Technology and Properties. *Reviews on Advanced Materials Science* **2014,** *38*, 75-93.

29. Vladislav, V.; Natalia, B.; Ruslan, G.; Philipp, L.; Yuri, L.; Yury, R.; Alexander, T.; Andrey, Z.; Yuri, S., Nature of V-Shaped Defects in GaN. *Jpn. J. Appl. Phys.* **2013,** *52*, 08JE14.

30. Northrup, J. E.; Neugebauer, J., Theory of GaN($10^{-}10$) and ($11^{-}20$) surfaces. *Physical Review B* **1996,** *53*, R10477-R10480.

31. Neugebauer, J., Ab initio Analysis of Surface Structure and Adatom Kinetics of Group-III Nitrides. *physica status solidi (b)* **2001,** *227*, 93-114.

32. Girgel, I.; Edwards, P. R.; Le Boulbar, E.; Allsopp, D. W.; Martin, R. W.; Shields, P. A. In *Investigation of facet-dependent InGaN growth for core-shell LEDs*, Proc. SPIE 9363, 2015; pp 93631V-93631V-8.

33. Kim, J.; Cho, Y.-H.; Ko, D.-S.; Li, X.-S.; Won, J.-Y.; Lee, E.; Park, S.-H.; Kim, J.-Y.; Kim, S., Influence of V-pits on the efficiency droop in InGaN/GaN quantum wells. *Optics Express* **2014,** *22*, A857-A866.

34. Horton, M. K.; Rhode, S.; Sahonta, S.-L.; Kappers, M. J.; Haigh, S. J.; Pennycook, T. J.; Humphreys, C. J.; Dusane, R. O.; Moram, M. A., Segregation of In to Dislocations in InGaN. *Nano Letters* **2015,** *15*, 923-930.

35. Duxbury, N.; Bangert, U.; Dawson, P.; Thrush, E. J.; Stricht, W. V. d.; Jacobs, K.; Moerman, I., Indium segregation in InGaN quantum-well structures. *Appl. Phys. Lett.* **2000,** *76*, 1600-1602.

36. Yoshida, H.; Kuwabara, M.; Yamashita, Y.; Uchiyama, K.; Kan, H., Radiative and nonradiative recombination in an ultraviolet GaN/AlGaN multiple-quantum-well laser diode. *Appl. Phys. Lett.* **2010,** *96*, 211122.

37. Dai, Q.; Schubert, M. F.; Kim, M. H.; Kim, J. K.; Schubert, E. F.; Koleske, D. D.; Crawford, M. H.; Lee, S. R.; Fischer, A. J.; Thaler, G.; Banas, M. A., Internal quantum efficiency and nonradiative recombination coefficient of GaInN/GaN multiple quantum wells with different dislocation densities. *Appl. Phys. Lett.* **2009,** *94*, 111109.

38. Bloom, S.; Harbeke, G.; Meier, E.; Ortenburger, I. B., Band Structure and Reflectivity of GaN. *physica status solidi (b)* **1974,** *66*, 161-168.

39. Xie, J.; Ni, X.; Fan, Q.; Shimada, R.; Özgür, Ü.; Morkoç, H., On the efficiency droop in InGaN multiple quantum well blue light emitting diodes and its reduction with p-doped quantum well barriers. *Appl. Phys. Lett.* **2008,** *93*, 121107.

40. Seong, T. Y.; Han, J.; Amano, H.; Morkoc, H., III-Nitride Based Light Emitting Diodes and Applications. *III-Nitride Based Light Emitting Diodes and Applications* **2013,** *126*, 171.

41. Feng, Z. C., *III-nitride devices and nanoengineering*. Imperial College Press: London, 2008; p xiv, 462 p.

42. Sang-Youp, Y.; Joon Heon, K.; Mun Seok, J.; Seung-Han, P.; Jongmin, L., Power Dependent Micro-Photoluminescence of Green-InGaN/GaN Multiple Quantum Wells. *Jpn. J. Appl. Phys.* **2011,** *50*, 050204.

43. Özgür, Ü.; Fu, Y.; Moon, Y. T.; Yun, F.; Morkoç, H.; Everitt, H. O.; Park, S. S.; Lee, K. Y., Long carrier lifetimes in GaN epitaxial layers grown using TiN porous network templates. *Appl. Phys. Lett.* **2005,** *86*, 232106.

44. Fukuda, M., *Optical semiconductor devices*. Wiley: New York, 1999; p xvi, 422 p.

45. Murotani, H.; Yamada, Y.; Honda, Y.; Amano, H., Excitation density dependence of radiative and nonradiative recombination lifetimes in InGaN/GaN multiple quantum wells. *physica status solidi (b)* **2015,** *252*, 940-945.

46. Zhang, Y.; Kappers, M. J.; Zhu, D.; Oehler, F.; Gao, F.; Humphreys, C. J., The effect of dislocations on the efficiency of InGaN/GaN solar cells. *Solar Energy Materials and Solar Cells* **2013,** *117*, 279-284.

Captions

Figure 1 (a) Cross-sectional STEM image of LED1's V-pits with MQW thinning on the $\{10\bar{1}1\}$ facets. (b) Cross-sectional STEM image showing LED2 MQWs with TD defects.

Figure 2 (a) Mean CL emission spectrum of LED1 generated from a 10 µm × 10 µm area hyperspectral map with (b), (c), (d) and (e) CL intensity maps corresponding to the color shaded regions marked on the spectrum.

Figure 3 (a) and (b) RT-CL intensity maps of the two LEDs, (c) and(d) CL Spectra of the annotated regions on the micrographs, (e) and (f) Correlation of centroid energy (between 2.4 – 3.2 eV) vs intensity (for LED1 and LED2, respectively).

Figure 4 Carrier generation rate dependence of (a) IQE (inset: IQE vs excitation power intensity (linear-scale)) and (b) peak energies (inset: FWHM vs G). PL spectra of (c) LED1 and (d) LED2 at high and low G.(e) the carrier dynamic and droop mechanism of LED1 as G increases.

Figure 5 TRPL temporal response at different excitation powers (~0.044– 0.76 MW/cm^2) of (a) LED1 and (b) LED2.

Figure 6 PL lifetimes of (a) LED1, and (b) LED2 as a function of G at 5K (black squares) and 290K (red circles). Insets are the radiative (blue squares) and non-radiative (magenta circles) lifetimes with respect to G at 290K.

For Table of Contents Use Only

Generated carrier dynamics in V-pit enhanced InGaN/GaN light emitting diode

Idris A. Ajia[†]; Paul R. Edwards[‖], Yusin Pak[†], Ermek Belekov[†]; Manuel A. Roldan[‡]; Nini Wei[‡]; Zhiqiang Liu[§], Robert W. Martin[‖] and Iman S. Roqan[†,*]

[†]King Abdullah University of Science and Technology (KAUST), Physical Science and Engineering Division, Thuwal, Saudi Arabia.

[‡]King Abdullah University of Science and Technology (KAUST), Imaging and Characterization Core Laboratory, Thuwal, Saudi Arabia.

[‖]Department of Physics, SUPA, University of Strathclyde, Glasgow, G4 0NG, United Kingdom.

[§]Development Center, Institute of Semiconductors, Chinese Academy of Sciences, Beijing, China.

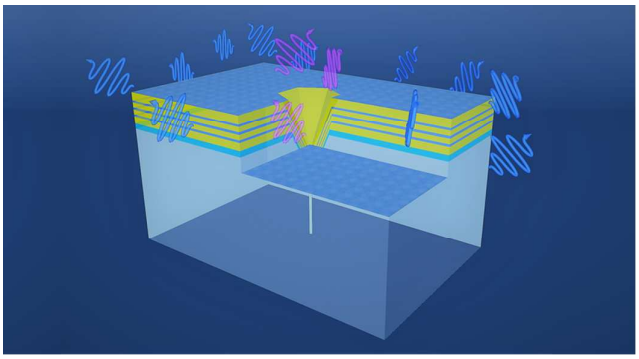

Synopsys: This graphic shows a V-pit with the different energy of photons emerging from the MQWs (low energy blue light) and the V-pits (high energy violet light)

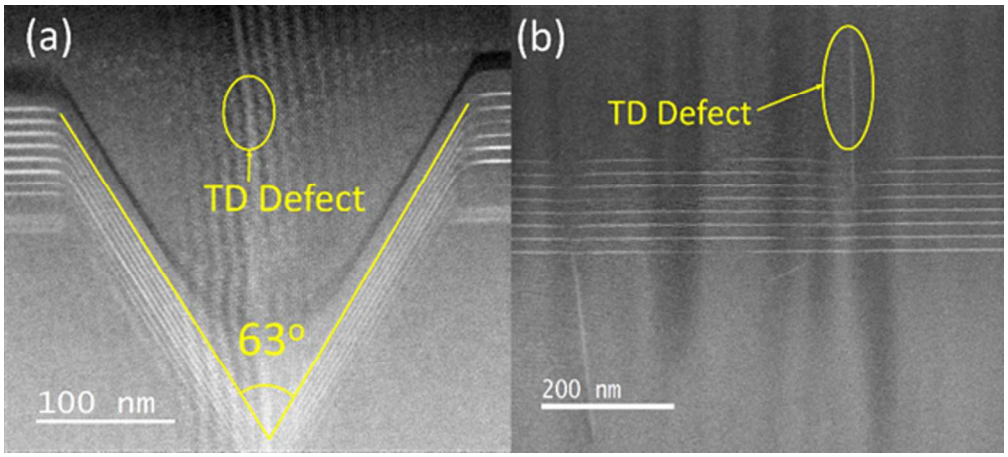

Figure 1 (a) Cross-sectional STEM image of LED1's V-pits with MQW thinning on the {101$\bar{1}$} facets. (b) Cross-sectional STEM image showing LED2 MQWs with TD defects.

83x37mm (300 x 300 DPI)

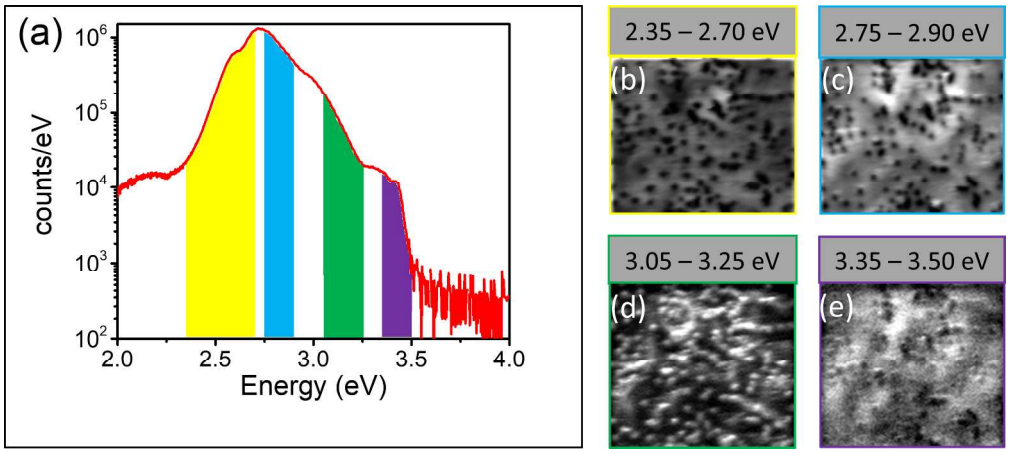

Figure 2 (a) Mean CL emission spectrum of LED1 generated from a 10 μm × 10 μm area hyperspectral map with (b), (c), (d) and (e) CL intensity maps corresponding to the color shaded regions marked on the spectrum.

988x437mm (72 x 72 DPI)

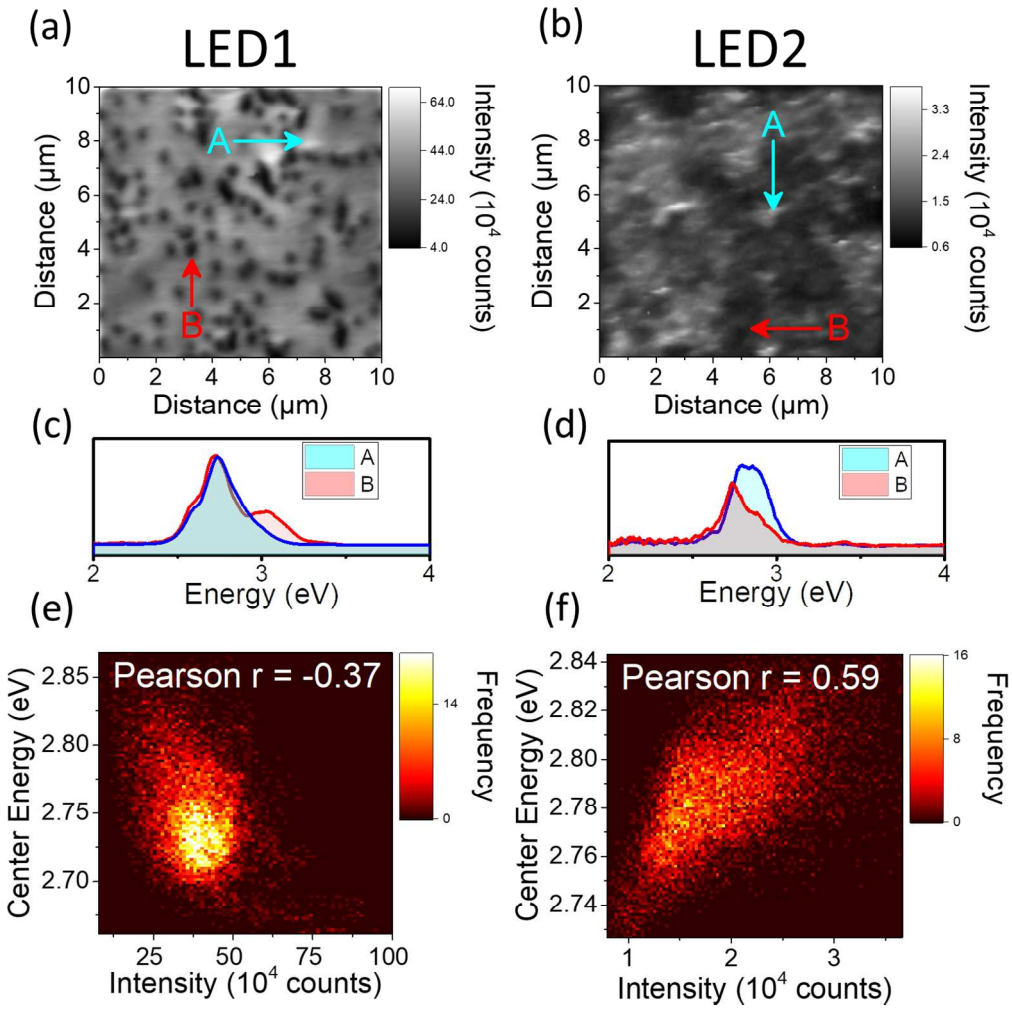

Figure 3 (a) and (b) RT-CL intensity maps of the two LEDs, (c) and(d) CL Spectra of the annotated regions on the micrographs, (e) and (f) Correlation of centroid energy (between 2.4 – 3.2 eV) vs intensity (for LED1 and LED2, respectively).

560x558mm (72 x 72 DPI)

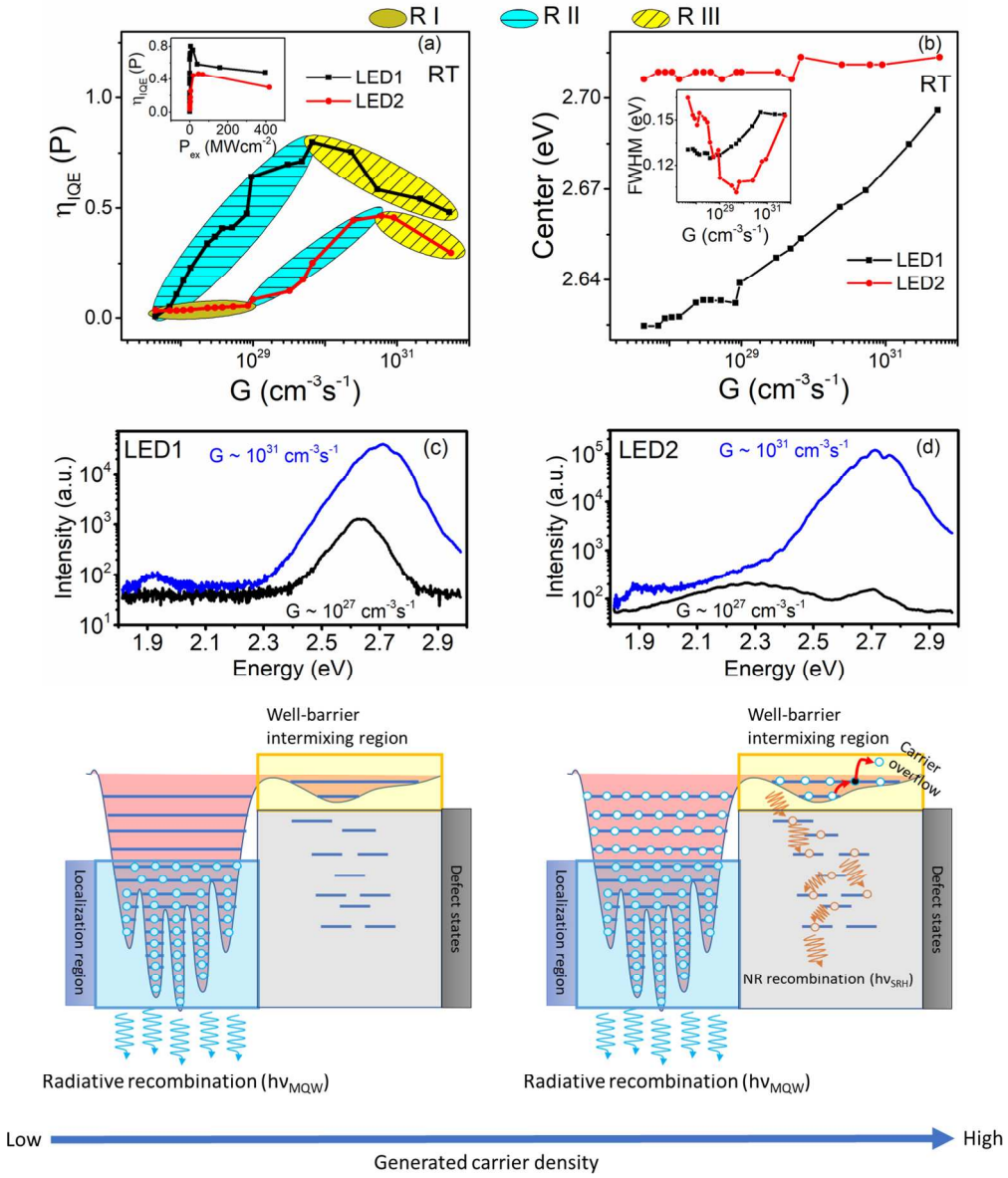

Figure 4 Carrier generation rate dependence of (a) IQE (inset: IQE vs excitation power intensity (linear-scale)) and (b) peak energies (inset: FWHM vs G). PL spectra of (c) LED1 and (d) LED2 at high and low G.(e) the carrier dynamic and droop mechanism of LED1 as G increases.

170x204mm (300 x 300 DPI)

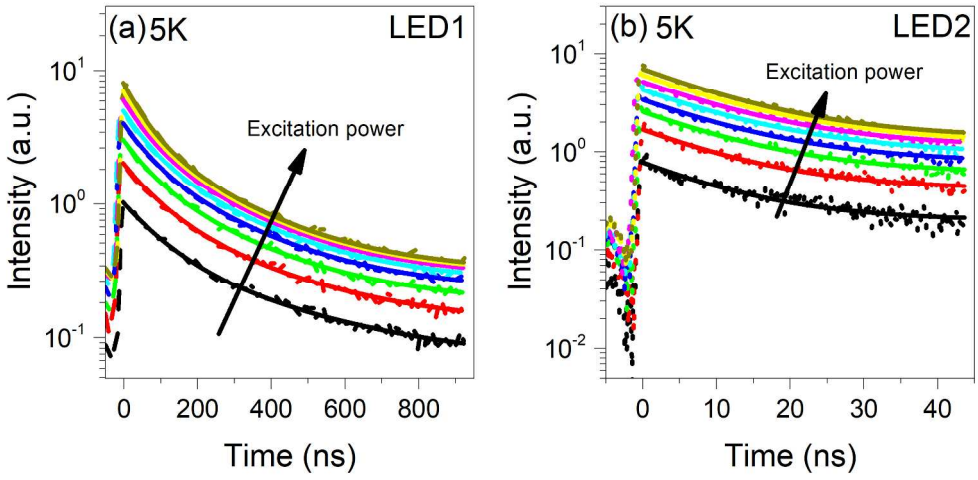

Figure 5 TRPL temporal response at different excitation powers (~0.044 – 0.76 MW/cm^2) of (a) LED1 and (b) LED2.

247x119mm (300 x 300 DPI)

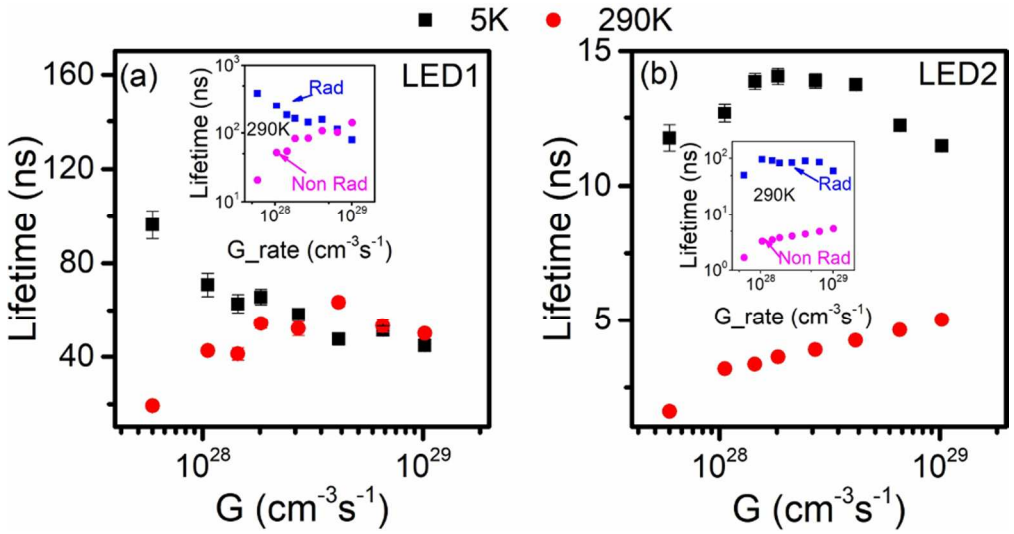

Figure 6 PL lifetimes of (a) LED1, and (b) LED2 as a function of G at 5K (black squares) and 290K (red circles). Insets are the radiative (blue squares) and non-radiative (magenta circles) lifetimes with respect to G at 290K.

85x44mm (300 x 300 DPI)

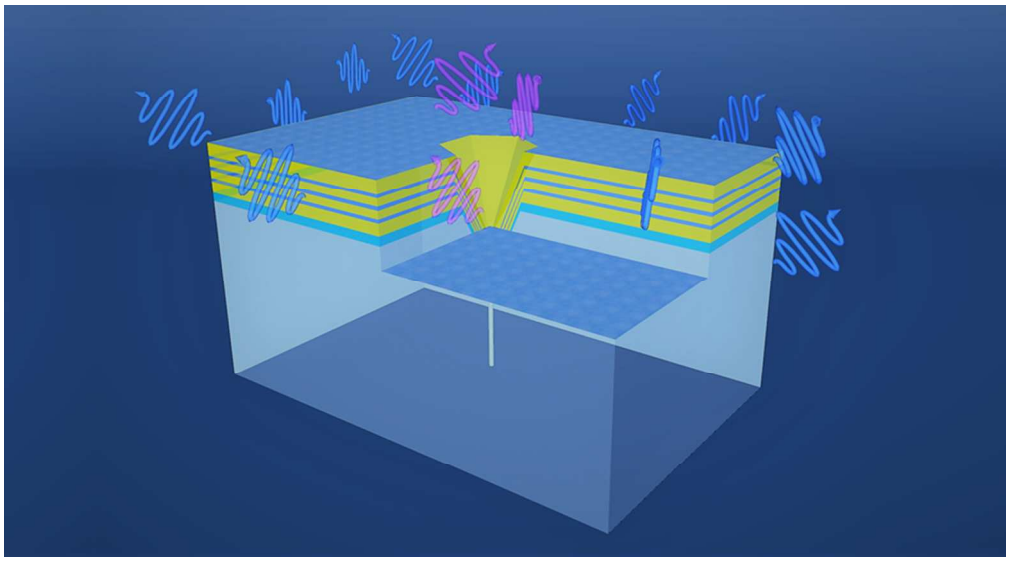

Table of Contents

88x48mm (300 x 300 DPI)